ELSEVIER

Available online at www.sciencedirect.com
ScienceDirect

C. R. Physique 9 (2008) 197–214

COMPTES RENDUS
PHYSIQUE

http://france.elsevier.com/direct/COMREN/

Recent developments in terahertz optoelectronics/Développements récents en optoélectronique térahertz

Tunable structures and modulators for THz light

Petr Kužel *, Filip Kadlec

Institute of Physics, Academy of Sciences of the Czech Republic, Na Slovance 2, 182 21 Prague 8, Czech Republic

Available online 9 January 2008

Abstract

We review recent results of both experimental and theoretical work aimed at developing tunable devices with optical properties in the THz range controllable by an external parameter. The presented devices include a semiconductor platelet, strontium titanate based elements and one-dimensional photonic crystals with defects. We show that it is possible to strongly modulate the complex permittivity in the THz range by light illumination, temperature and voltage, and the experimental results obtained by time-domain terahertz spectroscopy are found to be in a very good agreement with theoretical calculations. The control by illumination or applied bias enable a very fast modulation of the THz waves which is useful for prospect applications e.g. in the domain of communications. ***To cite this article: P. Kužel, F. Kadlec, C. R. Physique 9 (2008).***
© 2007 Académie des sciences. Published by Elsevier Masson SAS. All rights reserved.

Résumé

Structures accordables et modulateurs pour le rayonnement térahertz. L'article présente les résultats de travaux expérimentaux et théoriques récents ayant pour but de développer des dispositifs dont les propriétés optiques dans le domaine THz pourraient être contrôlés par un paramètre externe. Les dispositifs présentés incluent des lamelles de semiconducteurs, des éléments basés sur le titanate de strontium et des cristaux photoniques unidimensionnels comprenant des défauts. Il est démontré que la fonction diélectrique dans le domaine THz peut être fortement modulée par l'illumination par la lumière, les variations de température et de tension électrique ; les résultats expérimentaux obtenus par la spectroscopie térahertz dans le domaine temporel présentent un très bon accord avec les calculs théoriques. Grâce au contrôle par illumination ou par tension électrique, il est possible de moduler les ondes THz d'une manière très rapide, ce qui est utile pour les futures applications par exemple dans le domaine des communications. ***Pour citer cet article : P. Kužel, F. Kadlec, C. R. Physique 9 (2008).***
© 2007 Académie des sciences. Published by Elsevier Masson SAS. All rights reserved.

Keywords: Terahertz radiation; Tunable devices; Photonic crystals; Strontium titanate; Gallium arsenide

Mots-clés : Rayonnement térahertz ; Dispositifs accordables ; Cristaux photoniques ; Titanate de strontium ; Arsenure de gallium

1. Introduction

Generation and control of pulsed and continuous-wave freely propagating terahertz (THz) radiation have received considerable attention during last years [1–3]. Indeed, THz technology is a rapidly growing research field with a large impact on the semiconductor, superconductor, medical, space and defense industries; it starts to find applications in

* Corresponding author.
E-mail addresses: kuzelp@fzu.cz (P. Kužel), kadlecf@fzu.cz (F. Kadlec).

1631-0705/$ – see front matter © 2007 Académie des sciences. Published by Elsevier Masson SAS. All rights reserved.
doi:10.1016/j.crhy.2007.07.004

various tasks related to material inspection and communication. As more efficient THz sensors and sources become available, the speed of data acquisition becomes higher. Future short-range indoor communication systems may be designed for the sub-THz or THz range. We can expect a growing research emphasis put on manipulation of both guided and freely propagating THz beams by means of agile switches, modulators, phase shifters and tunable filters commanded either optically or electronically. All-optical devices allowing fast transfer of information from the optical spectral band to the THz band are, of course, of particular interest.

A device for the modulation of THz light can be described as a structure which contains a medium with a strong non-linear response. The word non-linear is used here in its most general sense meaning that the THz properties of this medium can be controlled by some external parameters (temperature, electric or magnetic field, light pulse, etc.). The structure may also contain a resonant element (e.g. a photonic crystal). As a rule, without a resonant element, a broadband response of the device can be achieved; however, a stronger non-linearity is required to obtain appreciable modulation effects. By contrast, the resonant element can dramatically enhance the non-linear interaction strength at the price of a significant narrowing of the useful bandwidth of the device. Both amplitude and phase modulation can be, of course, envisaged and this can be achieved through the modulation of the real or imaginary part of the permittivity (refractive index) of the tunable medium.

Ferroelectric materials are suitable for the modulation of the real part of the permittivity by controlling the bias electric field or temperature. Displacive ferroelectrics are characterized by the existence of a strong polar soft lattice vibrational mode responsible for the ferroelectric phase transition [4]. The contribution of the soft mode to the low-frequency dielectric permittivity is, as a rule, very high, owing to its strongly polar character and very low frequency. Under suitable conditions a high permittivity accompanied by reasonably low dielectric losses can be achieved even in the THz spectral range. The dynamics of the soft mode allows tuning of the dielectric permittivity by means of the temperature or the bias electric field [5]. In particular, so called incipient ferroelectric materials [4] such as strontium titanate ($SrTiO_3$, STO) or potassium tantalate ($KTaO_3$, KTO) exhibit a big potential for microwave and THz tuning. On the one hand, their THz response is fully controlled by a strong polar soft mode and, on the other hand, they remain in the paraelectric state down to the lowest temperatures. The current technology allows one to prepare high quality thin STO films which makes STO a material of choice for applications in tunable microwave components [5]. An increased tunability of STO-based structures in the microwave or THz range at room temperature can be achieved by chemical substitution of strontium atoms by barium (barium strontium titanate solid solutions) [5] or by introducing a tensile strain by a proper choice of substrate for the epitaxial thin film growth [6]. In particular, thin STO films grown on (110) $DyScO_3$ substrate were demonstrated to exhibit a ferroelectric phase transition close to the room temperature and, consequently, to show a highly enhanced dielectric tunability [6].

The usefulness of the high birefringence of liquid crystals for the control and manipulation of the light in the visible region is well known. The switching of the molecular orientation in (e.g. the nematic) liquid crystalline phase by an external electric or magnetic field is connected to the switching of refractive indices values. Recently a number of studies have shown that this property can be successfully used even in the THz and GHz spectral ranges both using the magnetic-field [7–10] and electric-field [11] modulation.

High-resistivity semiconductors show a big potential for opto-THz coupling. On the one hand, in their ground state, semiconductors are transparent and virtually dispersion free for the THz radiation. On the other hand, photo-excited semiconductors exhibit a strong interaction with the THz light which is mediated by free carriers. Generation of free carriers in a semi-insulating semiconductor induces a dramatic increase of the imaginary part of the permittivity and usually a small decrease of its real part in the THz spectral range. A fine tuning of the strength of interaction by the intensity of optical excitation then leads to interesting phenomena directly utilizable for THz-light modulation and switching [12–14]. Another interesting possibility consists in injecting free carriers into a semiconductor structure electronically [15]. Recently metamaterial structures were reported consisting of gold resonator elements with sub-wavelength dimensions deposited either on a doped *n*-GaAs thin film or on a ErAs/GaAs superlattice. The THz transmittance of the structure was controlled in the former case by an applied electric-field [16] and in the latter case by ultrashort optical pulses [17].

Photonic crystals (PCs) are periodic dielectric structures that may exhibit a so-called photonic band gap, i.e. a range of frequencies for which the propagation of light is forbidden [18]. At the same time, it is possible to enable the propagation of the electromagnetic waves in the band gap within a narrow line, so-called defect mode, by breaking the periodicity of the PC [18]. Although many applications and developments of these resonant structures have already appeared, some great challenges remain. Among them, the control of defect modes is of major interest for filtering ap-

plications, signal modulation, demultiplexing, etc. The design of controllable defect modes in PCs requires predictive formulas for the frequency dependence of the defect modes on their physical parameters. Numerical studies which must be conducted to describe two- and three-dimensional structures still remain quite challenging. In contrast, one-dimensional (1D) PCs enable a fully analytical theoretical description (and consequently, a deeper understanding of the defect mode formation) [19,20] and, at the same time, they are much easier to fabricate. A simple 1D PC consists of a stack of alternating dielectric layers of two materials with high and low refractive indices. A defective PC can be fabricated by inserting defect layer(s) into such a multilayer stack: a resonant mode then appears inside the band gap. In the case of a single defect layer such a 1D structure can be simply understood as a Fabry–Pérot (FP) resonator with periodic Bragg reflectors enclosing the layer. The defect layers can be made of material with a suitable nonlinear response, as pointed out above. Because of a high localization of the electric field at the defect mode frequency, a strong enhancement of optical nonlinearity can be expected within the defect layer. By applying the scaling laws [18], one can construct analogous 1D structures using suitable materials with appropriately scaled layer thicknesses from the optical down to the microwave spectral range: a number of functional 1D photonic structures based on FP resonator in various modifications and spectral ranges have been recently reported in the literature [21–26].

In this article we review our recent effort in the THz characterization of the dielectric tunability of STO-based structures, especially when inserted into 1D photonic crystals and of the opto-THz coupling mediated by free carriers in GaAs. In the majority of experiments we used time-domain terahertz spectroscopy (TDTS) setups which were described in detail in Refs. [27–30]; some experimental results were obtained using a coherent source (backward-wave oscillator) spectrometer [25]. In the paper we do not provide any further information about the experimental procedures for characterization of samples in the steady-state as these measurements are standard now in the THz range and the details can be found in the above cited references. On the other hand, we stress details of less standard experiments concerning the THz modulation induced optically or by means of external bias field.

The paper is organized as follows. In Section 2 we first provide a theoretical basis for the understanding of temperature and electric field tunability in the paraelectric phase of ferroelectrics. Subsequently we focus on STO and discuss the temperature and electric field control of its dielectric properties with the help of our experimental results obtained on STO single crystals and thin film structures. In Section 3 we show how the tuning of the losses in GaAs by optical excitation can be used for efficient modulation of the THz light. Finally, Section 4 is devoted to the description of one-dimensional photonic crystals and to the discussion of the properties of these structures with tunable defect layers made of incipient ferroelectrics and high-resistivity semiconductors.

2. External control of $SrTiO_3$ permittivity

2.1. Theoretical description

The high value of the dielectric permittivity of ferroelectrics in the paraelectric phase stems from a subtle compensation of microscopic forces between the atoms. As a result the compound remains unpoled in the absence of an electric field but the restoring force opposing the poling action of an applied electric field is weak. In displacive ferroelectrics this situation is accompanied by the presence of a polar soft transverse phonon mode which, according to the Lyddane–Sachs–Teller relation, dominates the low-frequency polar response of the material.

A straightforward evaluation of the dielectric response of ferroelectrics is provided by the conventional Landau–Devonshire theory. The Helmholtz free-energy density F can be expanded in a power series with respect to the components P_i of the macroscopic polarization vector. The lowest order terms of the development for the cubic paraelectric phase of STO then read [31,5]:

$$F(T)=\frac{1}{2}\alpha\left(P_x^2+P_y^2+P_z^2\right)+\frac{1}{4}\beta\left(P_x^4+P_y^4+P_z^4\right)+\frac{1}{2}\beta'\left(P_x^2P_y^2+P_y^2P_z^2+P_z^2P_x^2\right) \tag{1}$$

If an external electric field is applied with components E_i we can write a dielectric equation of state

$$E_i=\frac{\partial F}{\partial P_i} \tag{2}$$

which leads to (e.g. for the E_z component)

$$E_z=\alpha P_z+\beta P_z^3+\beta' P_z\left(P_x^2+P_y^2\right) \tag{3}$$

Analogous equations are found for the other two components of the field.

In STO (and generally in displacive ferroelectrics) the macroscopic polarization is essentially connected to the soft phonon mode, i.e. the contribution of the soft mode to the static permittivity $\delta\varepsilon(T)$ is highly dominant. In the paraelectric phase the spontaneous polarization vanishes and the macroscopic polarization is only induced by the electric field in agreement with Eq. (3). In our approximation we identify the macroscopic polarization introduced in Eq. (1) with that of the soft mode and, taking into account the equation of state (3), we can specify the coefficient α in the paraelectric phase as follows:

$$\alpha = \frac{1}{\varepsilon_{\mathrm{vac}}(\varepsilon_0(T) - \varepsilon_\infty)} \tag{4}$$

$\varepsilon_{\mathrm{vac}}$ is the vacuum permittivity, $\varepsilon_0(T)$ is a temperature dependent static relative permittivity of the material which can be obtained experimentally, and ε_∞ is a cumulative contribution of higher-frequency excitations (electronic contribution and higher frequency polar phonons):

$$\varepsilon_0(T) = \delta\varepsilon(T) + \varepsilon_\infty \tag{5}$$

The temperature dependence of ε_0 in the paraelectric phase usually obeys the Curie–Weiss law in a broad temperature range; in our case:

$$\varepsilon_0(T) = \frac{C}{T - T_0} + \varepsilon_\infty \tag{6}$$

In this paper we limit our analysis to the temperature range where the Curie–Weiss law is valid (i.e., $T \gtrsim 60$ K in STO). In a microscopic model the contribution of the soft polar phonon to the static permittivity is equal to

$$\delta\varepsilon = f/\omega_0^2 \tag{7}$$

where f is the oscillator strength (which is, as a rule, temperature independent) and ω_0 is the frequency of the transverse soft mode exhibiting the Cochran law:

$$\omega_0^2 = \frac{f}{C}(T - T_0) \tag{8}$$

The thermal tunability is then essentially related to the softening of the phonon frequency with temperature.

In contrast, the electric-field tunability is related to the anharmonicity of the Helmholtz potential as we show below. Eq. (3) provides the following expression for the relative dielectric permittivity ε_{zz}:

$$\begin{aligned}\varepsilon_{zz}(T) &= \frac{1}{\varepsilon_{\mathrm{vac}}}\frac{\partial P_z}{\partial E_z} + \varepsilon_\infty \\ &= \frac{\delta\varepsilon(T)}{1 + 3\beta\varepsilon_{\mathrm{vac}}\delta\varepsilon(T)P_z^2 + \beta'\varepsilon_{\mathrm{vac}}\delta\varepsilon(T)(P_x^2 + P_y^2)} + \varepsilon_\infty\end{aligned} \tag{9}$$

In the paraelectric phase the polarization vanishes in the absence of external field and $\varepsilon_{zz} = \varepsilon_0(T)$. If an external field E_z is applied the polarization P_z acquires a non-zero value following Eq. (3) and the actual value ε_{zz} of the permittivity is decreased compared to ε_0. Such a decrease can be attributed to the field-induced soft mode hardening. It follows from (7) and (9):

$$\omega_0^2(E_z) = \omega_0^2\left[1 + \frac{3\beta\varepsilon_{\mathrm{vac}}f}{\omega_0^2}P_z^2(E_z)\right] \tag{10}$$

This electric-field tuning effect is temperature dependent: it becomes more pronounced for the temperatures where the value of $\delta\varepsilon(T)$ itself is large (i.e., at low temperatures in STO).

Let us denote by E_0 a dc (or low-frequency) externally applied bias and by E_{THz} the THz probing field. Both fields are assumed to be parallel to the z-axis of the material; we put $E_z = E_0 + E_{\mathrm{THz}}$. After inverting Eq. (3) the first terms of the power expansion of the induced polarization at THz frequencies read:

$$P_z = \left(\frac{1}{\alpha} - 3\frac{\beta}{\alpha^4}E_0^2\right)E_{\mathrm{THz}} - 3\frac{\beta}{\alpha^4}E_0E_{\mathrm{THz}}^2 \tag{11}$$

The first term at the right-hand side of this equation accounts for the electric-field induced modulation of the linear permittivity, the second term describes a possible electric-field induced second harmonic generation process. These two nonlinear effects are described on the same basis by the anharmonic character of the free energy.

2.2. Temperature control

Although the soft mode dynamics and low-frequency permittivity in STO single crystals and thin films has been studied extensively [31–40] we have performed a temperature study of the STO single crystal by means of TDTS in order to get precise data on the dielectric dispersion of STO in the frequency range of our interest. Dielectric spectra we obtained using a 0.1 mm thick (100)-oriented STO single crystals platelet are shown in Fig. 1.

For the fits we applied a damped harmonic oscillator model representing the soft mode dispersion:

$$\varepsilon(\omega) = \varepsilon_\infty + \frac{f}{\omega_0^2 - \omega^2 - \mathrm{i}\omega\gamma} \tag{12}$$

As we access experimentally only frequencies below 2 THz, higher polar modes can be simply accounted for by a constant value of the high-frequency permittivity ε_∞ ($\approx$9.6 as it follows from the data in Refs. [41,42]). In the fits we considered very precise hyper-Raman scattering data [33] which provide the soft mode frequency ω_0 and damping γ versus temperature. The soft mode frequency ω_0 can be fitted using the Cochran law (8) which is closely related to the Curie–Weiss behavior of the static permittivity. One finds:

$$\omega_0(T)\left[\mathrm{cm}^{-1}\right] = \sqrt{31.2(T - 42.5)} \tag{13}$$

The soft mode damping γ then can be fitted by an empirical linear dependence

$$\gamma(T)\left[\mathrm{cm}^{-1}\right] = -3.3 + 0.094T \tag{14}$$

The numerical constants resulting from the fits can be successfully used in the 70–300 K temperature range and they also yield an excellent fit of our measured data (see fits in Fig. 1) if a temperature independent oscillator strength of $f = 2.3 \times 10^6\ \mathrm{cm}^{-2}$ is used in the model.

Thus the dielectric dispersion of STO single crystals in the THz range can be described with a very good precision by the damped harmonic oscillator model (12) and all the parameters of this model are quantified. In turn, Eq. (12)

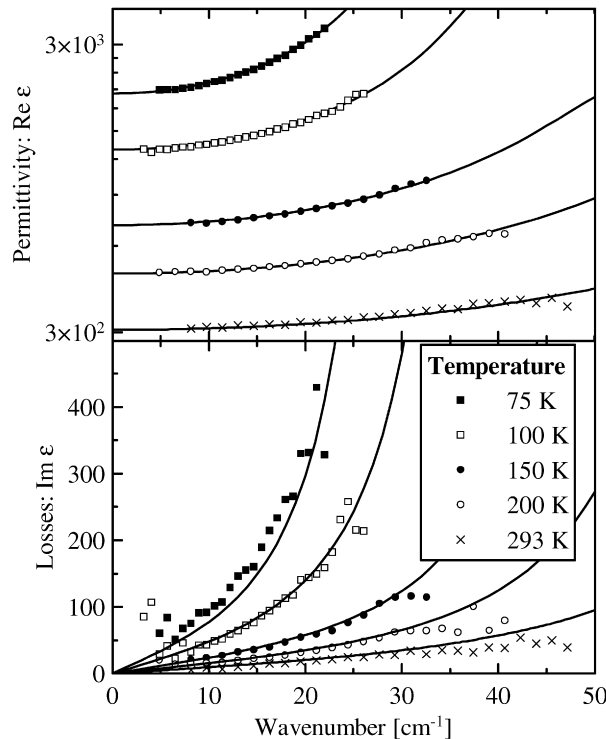

Fig. 1. Temperature dependence of the complex permittivity of STO single crystal as measured by TDTS. Solid lines represent fits by a temperature-dependent damped harmonic oscillator mode (see text).

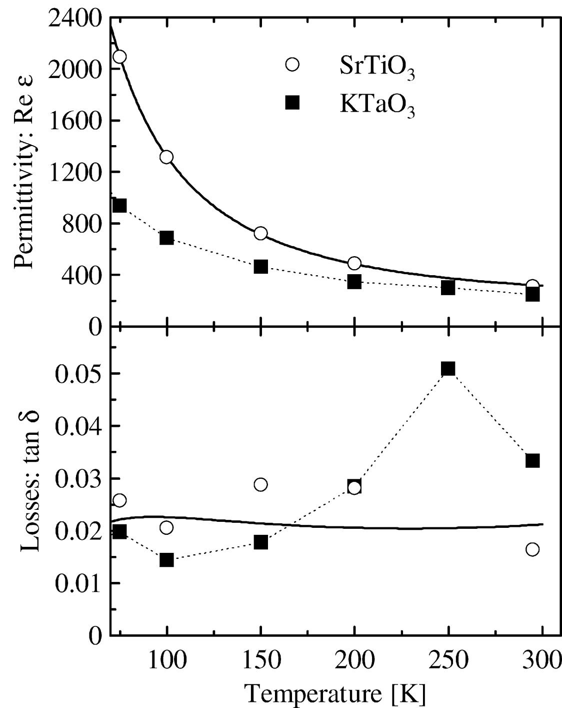

Fig. 2. Temperature dependence of the permittivity (ε) and the loss tangent ($\tan\delta$) of KTO and STO crystals at 0.2 THz. The data were measured using TDTS. The solid lines represent the fit by our model for STO; the dotted lines are guides for the eyes.

can be introduced into Eq. (9) to yield the expected electric-field tunability of STO in a wide range of temperatures. This requires also the knowledge of the constants β and β' characterizing the anharmonicity of the thermodynamic potential. The following estimations can be found in the literature [5,31]: $\beta \approx \beta' \approx 10^{10}\ \mathrm{J\,C^{-4}\,m^{-5}}$.

Fig. 2 shows a comparison of the thermal tunability and losses at sub-THz frequencies for two incipient ferroelectric materials we have studied experimentally: STO and KTO. The results show that the temperature dependent dielectric properties in the sub-THz range of the two compounds are not very different from each other. However, a higher tunability and permittivity value with comparable losses and a better mechanical properties brought us to select STO as the material for further investigation.

The THz properties of STO thin films differ in several aspects from those of single crystals [40,43,44,38]. First of all, the dielectric properties depend strongly on the quality of the thin film and can thus slightly differ from sample to sample. Nevertheless, it is possible to draw the general features characteristic for the thin films samples: (i) the damping of the soft mode in thin films is significantly higher namely owing to inhomogeneities and defects and (ii) the frequency of the soft mode does not soften so much as in the single crystal and it usually completely levels off below about 100 K [37,35,38].

2.3. *Electric field control*

The tuning of ferroelectric materials by means of applied electric field is widely used in the microwave range where such components find their use as capacitors, varactors, resonators, lens antennas, etc. [5]. However, with the ongoing increase of operating frequencies, the focus of interest shifts gradually towards the THz range. The nascent interest in this kind of device for future THz applications is testified for example by work demonstrating that an electric field can be used to shift the band gap in photonic crystals when an electro-rheological fluid is used as one constituent material [45].

For practical usage, devices with a high tunability are required; in the case of ferroelectric materials this necessitates applying a high electric field, of the order of tens of $\mathrm{kV\,cm^{-1}}$. To achieve such elevated values, it is possible either to use a high voltage connected to electrodes separated by a distance of the order of millimeters, or to apply a significantly

lower voltage while reducing the distance between the electrodes to some tens of microns. Within the former approach, the typical geometry is that of a parallel-plate capacitor. Its advantage is the relatively large volume influenced by the electric field which implies a stronger interaction with the propagating radiation; also, if the THz field propagates between the electrodes, the permittivity in both polarizations can be controlled as it follows from Eq. (9). In the latter case, the most convenient geometry is an interdigited capacitor structure which can be deposited on the surface of the ferroelectric material by lithography. As a great asset, the maximum useful cross-section is only limited by the size of the lithography mask, and a relatively low voltage of tens to hundreds of volts is sufficient to generate the high electric field; however, because of the THz-light polarizing properties of the electrode structure, only linearly polarized radiation with the E-vector perpendicular to comb-shaped electrodes can be used.

In our experiments we have employed the interdigited capacitor geometry—a 20 nm Ti/300 nm Au stack metal film was deposited on the surface of STO by magnetron sputtering; subsequently, the electrodes were formed using photolithography and ion beam etching. The resulting structure consisted of 5 μm wide metal stripes separated by 15 μm wide gaps. The total area covered by the electrode structure was about $6 \times 6\ \text{mm}^2$. In order to determine the tuning behavior of the ferroelectric thin films, a quasi-static ac voltage ($f = 166$ Hz) was applied to the contact pads, and a synchronous detector locked to its frequency was used. By this detection mode, the sensitivity of the experiment was considerably enhanced with respect to the usual setup using a mechanical chopper.

In the first series of experiments we studied room-temperature tuning properties of three different ferroelectric thin films structures: (i) STO with a thickness of 310 nm on an r-cut sapphire substrate; (ii) 300 nm thick $Ba_{0.7}Sr_{0.3}TiO_3$ (BST) film on r-cut sapphire substrate; and (iii) a multilayer stack comprising 20 bilayers of STO/$DyScO_3$ 10 nm films (with a total thickness of 400 nm) deposited on $DyScO_3$ substrate. While the tunability of the STO thin film is determined by its intrinsic properties, one can expect a tunability increase either upon chemical substitution of Sr by Ba atoms due to the increase of the Curie temperature [46], or owing to a tensile lattice strain as in the case of the STO/$DyScO_3$ multilayer [6].

For studying the tuning properties of the samples the electrode structures were oriented such that the electric field vector of the incident THz beam was perpendicular to the metallic stripes. The reference measurement was performed with zero applied bias and the synchronous detection locked to the frequency of a mechanical chopper: the corresponding THz waveform is denoted as $E_{\text{THz}}(0)$. Subsequently, the chopper was removed from the beam path and the detection was synchronized with the applied ac voltage as described above. In this case the measured waveforms are proportional to the voltage-induced change of transmitted THz field, $\Delta E_{\text{THz}}(V) = E_{\text{THz}}(V) - E_{\text{THz}}(0)$. As a rule, even if the highest amplitudes of the applied voltage are used, the maximum values of ΔE_{THz} amount to a few percent of the zero-bias THz field. Given such a small modulation of the THz signal, it is possible to calculate the field-induced change of the complex refractive index of the film using the first order development:

$$\Delta N(\omega) \approx \frac{\Delta t(\omega)}{\mathrm{d}t/\mathrm{d}N} = \frac{\Delta E_{\text{THz}}(\omega; V)}{E_{\text{THz}}(\omega; 0)} \frac{t}{\mathrm{d}t/\mathrm{d}N} \tag{15}$$

We denote by $N = n + \mathrm{i}\kappa$ the complex refractive index of the sample in equilibrium. For STO and BST samples where a single film was deposited onto the substrate, the derivative $\mathrm{d}t/\mathrm{d}N$ can be calculated using a standard expression for the transmission through a thin film on substrate [47]:

$$t(\omega) = \frac{4N \exp[\mathrm{i}\omega N d/c]}{(1+N)(N+N_{\mathrm{s}}) + (1-N)(N-N_{\mathrm{s}})\exp(2\mathrm{i}\omega N d/c)} \tag{16}$$

where c denotes the vacuum light speed, N_{s} is the refractive index of the substrate, and d is the thickness of the film. For the STO/$DyScO_3$ multilayer stack the evaluation of experimental results has to be performed numerically. The transmission function of the multilayer stack and its derivative are calculated using the transfer matrix formalism briefly described in Section 4.1 assuming that the layers of $DyScO_3$ exhibit the dielectric properties of the bulk single crystal.

This approach yields the electric-field induced variation of the refractive index (or equivalently of the permittivity) averaged over the volume of the thin film(s); the presence of interdigited electrodes is not taken into account as they diminish the transmittance both in the zero-bias and voltage-dependent measurements in the same manner.

Representative results of relative tunability of the three studied thin films, obtained with an applied electric field of $65\ \text{kV}\,\text{cm}^{-1}$ are shown in Fig. 3, where we have introduced the following notation: the equilibrium permittivity is $\varepsilon = \varepsilon_1 + \mathrm{i}\varepsilon_2$ and the electric-field induced permittivity change is $\Delta\varepsilon = \Delta\varepsilon_1 + \mathrm{i}\Delta\varepsilon_2$.

In the case of a single STO layer, we have shown [48] that the observed behavior can be explained by the hardening of the soft mode frequency which leads to a decrease in the static permittivity value. The complex permittivity, both without and with the applied voltage, can be well accounted for by a model of dielectric function with a single harmonic oscillator describing the soft mode [see Eq. (12)]. At zero bias field the soft mode is heavily damped ($\gamma \approx 100\ \text{cm}^{-1}$)—this is probably due to inhomogeneous broadening which is frequently observed in thin films—with its eigenfrequency lying around 90 cm^{-1}. The data displayed in Fig. 3 obtained for a bias field of 65 $\text{kV}\,\text{cm}^{-1}$ can be explained by hardening of the soft mode by about 2 cm^{-1}. The fact that upon applying the voltage, the $\Delta\varepsilon_1$ is negative (i.e. the permittivity value decreases) in the low-frequency part of the spectrum and positive (i.e. the permittivity increases) in its high-frequency part is related to the heavily damped character of the soft mode. The value at 1 MHz plotted in Fig. 3 was obtained by impedance spectroscopy [48] and indicates that there is no additional dielectric contribution to the tuning in between the MHz and THz spectral ranges. The negative differential losses are in agreement with the soft mode hardening and they display a decrease in the whole frequency range.

In the case of the BST sample, which is in fact in the ferroelectric phase at room temperature, a slightly better tunability than with STO was observed below 0.3 THz. The soft mode is overdamped; this manifests itself in the real part of the permittivity which decreases with applied field in the whole THz range. An especially marked decrease occurs below 0.25 THz where the dispersion towards the MHz frequencies is considerably higher than for STO. In this frequency domain, the decrease in the imaginary part is also substantially higher than for STO while above 0.7 THz, $\Delta\varepsilon_2/\varepsilon_1$ of BST and STO are comparable. All these findings indicate high losses of the film in the THz and GHz frequency ranges.

Of the three samples under study, the best tunability was measured in the case of the STO/DSO multilayer. The sample was opaque in the frequency range above 1.2 THz due to an increased absorption of $DyScO_3$ substrate as compared to sapphire substrate. Below this limit, a roughly linear increase of the real part tunability was observed. Similarly as for a single STO layer on sapphire, the complex permittivity of STO in the multilayer sample, both without and with the applied voltage, can be described by a single damped harmonic oscillator model. While the soft mode damping is similar to that observed in a single STO layer, the soft mode eigenfrequency is significantly

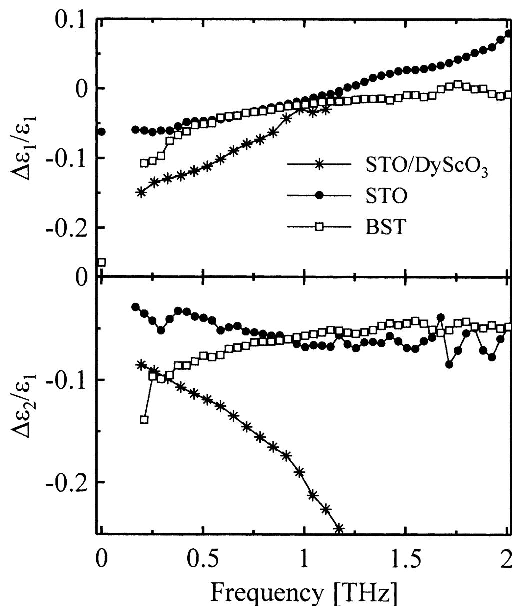

Fig. 3. Comparison of the room-temperature tunability for various ferroelectric thin films at an applied electric field of 65 $\text{kV}\,\text{cm}^{-1}$. The isolated symbols near zero frequency were obtained by impedance spectroscopy.

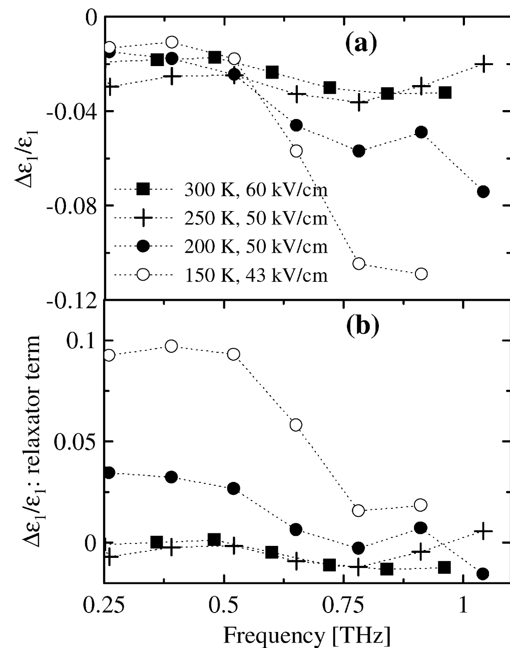

Fig. 4. (a) Temperature dependence of tunability of the bulk STO sample: experimental data. (b) Difference between the experiment and the model calculations based on the soft mode hardening. The non-zero values are interpreted as a contribution of a relaxational process (see text).

decreased due to the tensile stress induced by the lattice constant mismatch with $DyScO_3$ substrate and films. [6] At zero field the soft mode frequency lies at about 58 cm^{-1}; its shift induced by a bias field of 65 kV cm^{-1} is as high as 5 cm^{-1} (the shift amounts to 2 cm^{-1} for a single layer STO). These results confirm the positive influence of lattice strain on the tunability of STO.

In a second series of experiments we studied the temperature dependence of tuning properties of bulk STO. In bulk crystal, on the one hand, the value of losses is expected to be lower than in the case of thin films where inhomogeneous broadening increases the damping of the soft mode [38]; on the other hand, it is difficult to prepare a very thin platelet of a single crystalline sample so the bulk absorption may be substantially higher than that obtained in the thin film simply due to the sample thickness. For our measurements, the electrode structure was deposited onto a 50 μm thick single crystal platelet; the sample was placed in an optical cryostat equipped with electrical connections for applying the voltage to the sample. An ac voltage with a rectangular time profile was used to bias the sample; in parallel, the residual current, which was of the order of 1 mA, was monitored in order to prevent the dielectric breakdown on the sample surface.

The experimental data from bulk STO were evaluated by the same procedure as in the case of thin films; we made the assumption that with the applied electric field, the volume influenced by the field can be approximately regarded as a thin layer. In order to estimate its thickness, we have used an electrostatic simulation of the field distribution which yielded a value of 3 μm corresponding to the mean field penetration depth. The results for temperatures between 150 and 300 K are shown in Fig. 4. One can see in Fig. 4(a) that at frequencies close to 1 THz, the tunability increases upon cooling; this is in accordance with the decrease of the soft mode frequency [cf. Eqs. (7) and (9)].

Surprisingly, the tunability is substantially reduced in the low-frequency part of the spectrum—one can observe a pinning of the static permittivity value which cannot be described simply by a change of parameters of the soft mode. Indeed, using the model presented in Section 2.1 and the numerical values of parameters given in Section 2.2 we can calculate (without any fitting parameter) the expected response of STO under the bias field. Fig. 4(b) shows the difference between the measured values displayed in Fig. 4(a) and the results of the model calculations. At high temperatures (250 and 300 K) the soft-mode model fits well the data within the experimental error. At 200 and 150 K we observe a progressive increase of additional contribution below 0.75 THz (25 cm^{-1}) while the high-frequency part of the spectrum seems to converge to the soft mode model. The offset between $\Delta\varepsilon_1/\varepsilon_1$ at lower and higher frequencies can be presumably described by a relaxator term which almost compensates at low frequencies the entire change induced by the soft mode. The microscopic origin of this relaxation is not yet clear; we suppose that it might be related to the motion of charged crystal defects close to the electrodes under the influence of the applied voltage, which would lead to their non-homogeneous distribution along the sample surface. Further investigation is required to understand the tuning mechanism in more detail prior to preparation of structures suitable for real applications.

3. Tuning of losses in gallium arsenide

Undoped semiconductor materials are suitable for tunable devices owing to the fact that in the ground state, they are completely transparent for the THz radiation, whereas photoexcitation of electrons from the valence to the conduction band leads to a marked increase in the index of absorption in the THz range. This makes it possible to set up relatively simple opto-THz switches where the propagation of THz waves is controlled by visible light. For an efficient control, the incident photon energy has to exceed the band gap energy; the intensity of the optical pump will determine the concentration of the free charge carriers and consequently also the value of the THz index of absorption. Two time regimes of modulation can be envisaged: a pulsed and a continuous-wave (cw) one. The lifetime of free carriers is an important parameter for both these regimes. It determines the maximum switching rate in the former case, i.e. a sub-ns lifetime (like that observed in GaAs) is suitable for applications requiring fast response [49]. On the other hand, semiconductors with a long carrier lifetime like silicon can be suitable for a slow modulation or attenuation of cw sources [50,51]: in this regime the long lifetime allows one to reduce considerably the threshold optical pump intensity which induces an appreciable modulation of the THz beam; this fact is then counterbalanced by a lower operation rate.

For our studies we have used undoped GaAs where the lifetime of free electrons is of the order of hundreds of picoseconds. This suppresses an unwanted diffusion of carriers in the semiconductor and leads to an agile behavior where the switch can change its properties with sub-ns speed. Also, the energy of band gap of GaAs, 1.42 eV, suits ideally for photoexcitation by a Ti:sapphire laser.

3.1. Theoretical description

We have used a configuration based on a single crystalline GaAs plate; the optical beam is incident on its surface from the free space, while the THz pulsed radiation reflects under normal incidence at the same surface from inside. Without illumination, the THz pulses reflect according to usual Fresnel relations for a single interface.

When the surface of the crystal is illuminated by an optical beam with a homogeneous lateral intensity profile, a distribution of free electrons and holes arises within a thin layer below the surface. For simplicity, it is possible to consider the concentration of free carriers to be constant up to some thickness and then drop to zero. Then, the model consists of three media with two plane-parallel interfaces: (i) the undoped semiconductor in the ground state described as a lossless medium filling the half-space of the incident THz wave and characterized by a real refractive index $N_0 = n_0$; (ii) the photoexcited part of the semiconductor with a thickness d_1 and complex refractive index $N_1 = n_1 + \mathrm{i}\kappa_1$; and (iii) a half-space filled by air where the wave is transmitted and $N_2 = n_2 = 1$. At normal incidence, the amplitude reflection coefficient of this structure is equal to [47]

$$r = \frac{r_{12}\exp(2\mathrm{i}\omega N_1 d_1/c) - r_{10}}{1 - r_{10} r_{12}\exp(2\mathrm{i}\omega N_1 d_1/c)} \tag{17}$$

Here c denotes the vacuum light speed, ω is the THz field frequency and r_{ij} are the Fresnel amplitude reflection coefficients at the interfaces between media i and j. The thickness d_1 is chosen to be equal to the penetration depth of the pump beam; the refractive index N_1 depends on the wavelength and intensity of the optical pump.

Using this formula, it is possible to deduce that upon the variation of excitation intensity, the reflection coefficient goes through three main regimes which can be understood easily:

- Without external pumping, virtually all electrons remain in the valence band; the above equation reduces to the standard expression for reflectance on a single interface which, for GaAs, amounts to about $r = 0.3$.
- At moderate pump intensity, the photoexcited layer can have antireflection properties so that $r \approx 0$; this occurs if the numerator of Eq. (17) is equal to zero, i.e.

  $$N_1 \approx \left[\frac{(n_0 - 1)c}{2\omega d_1}\right]^{1/2}(1 + \mathrm{i}) \tag{18}$$

  this condition is valid provided that the layer is sufficiently thin, $d_1 \ll c/(2\omega|N_1|)$ which is true at low or moderate pump fluences [30].
- As the pump intensity is further raised the reflectance undergoes an increase, too. This is due to the fact that the higher concentration of free electrons turns the photoexcited layer opaque and its optical response in the THz range becomes metal-like. The reflection of the THz pulses occurs predominantly on the interface between unexcited bulk GaAs and the conductive photoexcited layer; as the pulses in this case pass from an optically thinner medium to a denser one, the phase of the radiation experiences a phase-shift by π with respect to the reflection at the unexcited interface where the radiation passes from an optically denser medium to a thinner one (i.e. air). This phase shift can be detected in TDTS as a change of sign in the measured waveform $E(t)$. Finally, for a sufficiently high pumping power, the reflectance comes close to unity.

Thus, by varying the optical power, the inner reflectance at THz frequencies can be tuned in a wide range. The THz properties of photo-excited semiconductors can be usually well described by the Drude model [52]:

$$N_1 = \left(\varepsilon_\infty - \frac{\omega_p^2}{\mathrm{i}\omega\Gamma + \omega^2}\right)^{1/2} \tag{19}$$

where the plasma frequency of the free carriers (with charge e, density N_e and effective mass m) is equal to:

$$\omega_p = \sqrt{\frac{N_e e^2}{m\varepsilon_{\mathrm{vac}}}} \tag{20}$$

where Γ is the momentum scattering rate of the charges, and ε_∞ is the permittivity of unexcited semiconductor.

The behavior of the complex THz refractive index versus carrier density is then characterized by an increase of the value of κ_1 and by a crossing of n_1 and κ_1 in the range 10^{15}–10^{17} cm^{-3} for the most common semiconductors like

GaAs, InP or Si. The values of the crossing can be quite close to those required by the condition (18) depending on the optical and THz frequencies used. This corresponds to the anti-reflective regime. For higher carrier densities κ_1 further increases and the photoexcited layer behaves like a thick conductive reflector with $d_1 > c/(2\omega\kappa_1)$.

The simple analytical model introduced above provides a clear insight into the underlying physics of the problem. However, using a numerical simulation of the THz beam reflection, it is possible to obtain a more accurate model without the need to simplify the properties of the photoexcited sample by assuming the step-like excitation profile. We used a method described in Ref. [53] assuming a linear absorption regime and negligible carrier diffusion on the picosecond time scale (resulting in an exponential profile of free carrier density along the surface normal) and a Drude-like dynamics of photoexcited electrons and heavy-holes probed by the THz radiation. We found that the analytical model is in a good agreement with the numerical calculation. It significantly differs from the numerical one (overestimates the reflectance) only for very high carrier densities and in the case of a low pump pulse absorption (thick photoexcited region) [14].

3.2. Experimental realization

As a source of femtosecond laser pulses, we have used a Ti:Sapphire laser amplifier with a 1 kHz repetition rate providing 50 fs pulses with a mean wavelength of 810 nm and energy of 1 mJ per pulse. The pulse train was split into three branches—one used for photoexcitation, one for generation of THz pulses via optical rectification on a 1 mm thick ZnTe crystal, and one for electro-optic sampling of the THz radiation.

For measurements of internal reflectance of GaAs, we have used a plane-parallel slab of a semi-insulating GaAs crystal with a thickness of 350 μm. The sample was attached to a circular opening with a 3 mm clear aperture and held in the common focus of two ellipsoidal mirrors reflecting the THz radiation. The pump beam excited an area with a diameter of 5 mm, and the pump fluence was varied between 0.8 and 200 μJ cm^{-2} using neutral density filters. Both beams were directed from the same side (see Fig. 5) and the photoexcitation of the surface of the GaAs wafer occurred only after the THz pulse has passed through into the bulk of the sample. Under these conditions the FP-like reflections

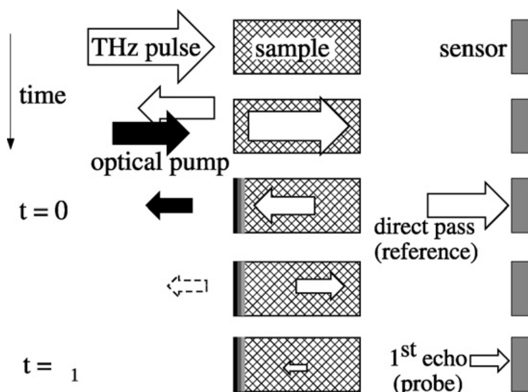

Fig. 5. The time sequence of pulses and their propagation through the sample (drawn out of scale). The area of arrows symbolizes the relative pulse energy.

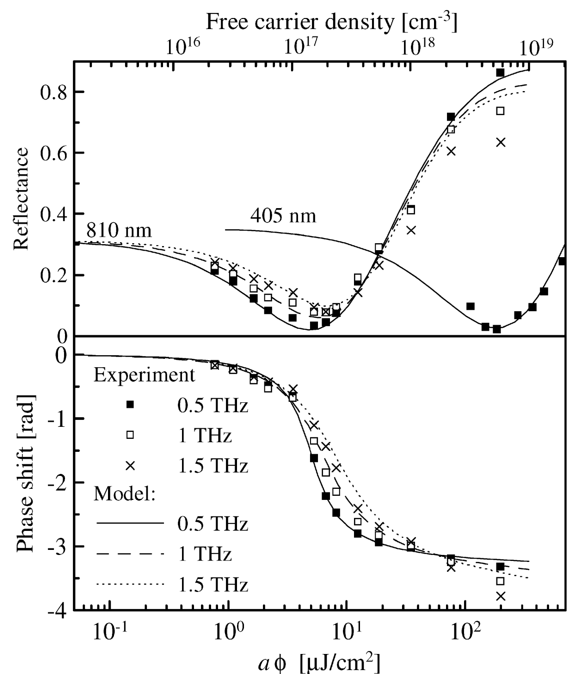

Fig. 6. Power reflectance and phase shift of the internally reflected THz wave versus incident optical pump fluence ϕ and the corresponding free carrier density for two optical wavelengths ($a = 1$ for 810 nm and $a = 0.5$ for 405 nm) in GaAs.

of the THz beam inside the GaAs wafer made it possible to determine the internal reflectance with a phase sensitivity (see also Ref. [30] for more details). An advantage of this arrangement is the possibility to perform the measurement of reflectivity including the reference measurement in a single run.

The experimental results of reflectance and phase shift, together with the curves obtained from numerical simulations are shown in Fig. 6; both are found to be in an excellent agreement. One can see that the reflectance displays a slight dispersion in the THz range—for example, both the theoretical and experimental values of the fluence for which we observe the reflectance minimum show a small variation with the probing THz frequency. In fact, the carrier concentration where the reflectance minimum occurs depends on the ratio between the THz wavelength and the penetration depth of the optical beam as it can be seen in the frequency-dependence of Eq. (18). Also the power reflectance itself reaches lower values (antireflective behavior) for lower frequencies; by contrast, at high pump fluence, the lower frequencies are better reflected than higher ones. Thus, the best tuning performance among the frequencies shown can be obtained for the probing frequency 0.5 THz, where the power reflectance attains values ranging from 3 to 85 percent.

4. One-dimensional photonic crystals with defect modes

4.1. Theoretical description

A one-dimensional PC with a defect can be considered as a thin FP cavity surrounded with two Bragg mirrors ensuring an optical feedback. A convenient theoretical approach is based on the transfer matrix formalism [53,20]. In this approach, amplitudes of p- and s-polarized electric field components of forward ($E_{\rightarrow}$) and backward ($E_{\leftarrow}$) propagating waves at the interfaces between adjacent layers (i.e. at planes z_j and z_{j+1} of the layered structure) are connected through the transfer matrices (see Fig. 7):

$$\begin{pmatrix} E_{\rightarrow}(z_{j+1}) \\ E_{\leftarrow}(z_{j+1}) \end{pmatrix} = M_j \begin{pmatrix} E_{\rightarrow}(z_j) \\ E_{\leftarrow}(z_j) \end{pmatrix} \tag{21}$$

The product of all the transfer matrices M_j ($j = 0, \ldots, n-1$) describing individual layers of a stack yields the transfer matrix M of the whole block. Assuming that the structure is only composed of nonabsorbing media it can be

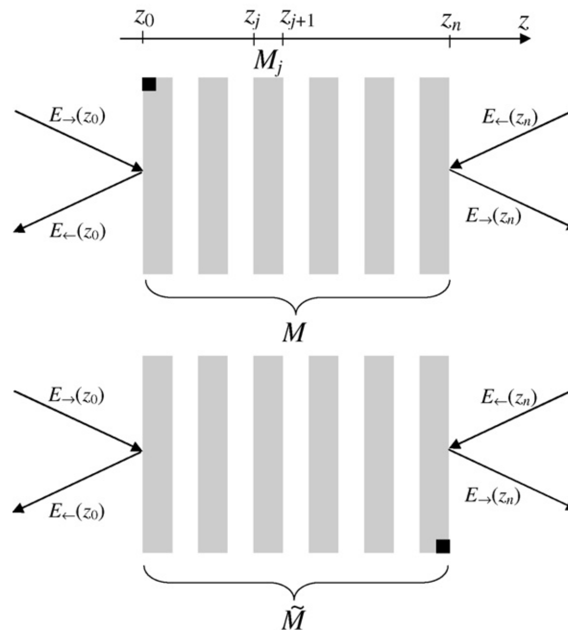

Fig. 7. Schematic definition of fields and symbols used in the description of the transfer matrix method. The transfer matrix $\tilde{M}$ describes the structure which was created by a 180° rotation of the upper one around the axis perpendicular to the plane of incidence.

shown that its transfer matrix can be simply related to the complex transmittance $t\exp(\mathrm{i}\tau)$ and reflectance $r\exp(\mathrm{i}\rho)$ coefficients:

$$M = \frac{1}{t}\begin{pmatrix} \exp(-\mathrm{i}\tau) & r\exp[-\mathrm{i}(\rho-\tau)] \\ r\exp[\mathrm{i}(\rho-\tau)] & \exp(\mathrm{i}\tau) \end{pmatrix} \tag{22}$$

These transmission and reflection coefficients can be obtained experimentally: if the structure is illuminated, e.g., from the left-hand side we identify the incident E_i, reflected E_r and transmitted E_t fields with the fields shown in the upper part of Fig. 7 as follows: $E_{\rightarrow}(z_0) \equiv E_i$, $E_{\leftarrow}(z_0) \equiv E_r$, $E_{\rightarrow}(z_n) \equiv E_t$, and $E_{\leftarrow}(z_n) = 0$, i.e.,

$$\begin{pmatrix} E_i \\ E_r \end{pmatrix} = M \begin{pmatrix} E_t \\ 0 \end{pmatrix} \tag{23}$$

If, conversely, the incident wave impinges on the structure from the right-hand side we get $E_{\rightarrow}(z_0) = 0$, $E_{\leftarrow}(z_0) \equiv E_t$, and $E_{\rightarrow}(z_n) \equiv E_r$, $E_{\leftarrow}(z_n) \equiv E_i$. This case can be alternatively described by a transfer matrix $\tilde{M}$ (see lower part of Fig. 7) with complex field transmittance $\tilde{t}\exp(\mathrm{i}\tilde{\tau})$ and reflectance $\tilde{r}\exp(\mathrm{i}\tilde{\rho})$. One can easily show that $\tilde{t} = t$, $\tilde{\tau} = \tau$, $\tilde{r} = r$, and $\tilde{\rho} = 2\tau - \rho + \pi$.

As already pointed out, this description is important from the experimental point of view: the transfer matrix of a given structure can be obtained directly from the transmission and reflection experiments. The phase sensitivity of TDTS is here a big advantage. Complex structures can be decomposed into several suitable building blocks which can be characterized separately. For example, our PC with a defect can be decomposed into two outer periodic Bragg mirrors (denoted by indices A and B) and the inner defect part (index D). Each block then can be described in terms of its transfer matrix (22): M_A, M_B, and M_D. In principle, the transfer matrix of any block can be calculated if its own properties (i.e. thickness, refractive index, and wave impedance of each of its constituting layers) are known. However, in practice these microstructure data are not always available and/or the real microstructure can somewhat differ from the nominal one. In this case phase-sensitive measurements of the complex reflection and transmission coefficients can provide complete information about each building block. In the ideal case, the two Bragg mirrors have identical properties as they are assumed to have the same microstructure but it is not a requirement as their experimental realizations can show different properties from the predicted ones to some extent. These possible differences can be detected in the transmission and reflection experiments and the corresponding transfer matrices then could display slightly different coefficients.

Hence the properties of an entire general structure can be predicted before it is built from the blocks without an exact knowledge of the microstructure details. Note that we express the transfer matrices in terms of experimentally accessible quantities, i.e., the reflectance and transmittance of the separate blocks surrounded by the air. One can easily show that the transfer matrix of two such blocks—e.g. M_A and M_D—put into optical contact reads simply $M_A \cdot M_D$.

Depending on the optical properties of the defect, our structure may display a defect mode characterized by a narrow range of frequencies in the forbidden band for which the propagation through the structure is allowed (i.e. $t \rightarrow 1$ in a structure composed of lossless materials). In the limit of perfect outer Bragg structures ($r_A \rightarrow 1$ and $r_B \rightarrow 1$) the defect mode condition $t = 1$ yields [29]:

$$2\tau_D = 2\pi m - (\tilde{\rho}_A + \rho_B) + 2\arg\bigl\{1 - r_D \exp\bigl[\mathrm{i}(\tilde{\rho}_A + \rho_B + \tilde{\rho}_D + \rho_D)/2\bigr]\bigr\} \tag{24}$$

where m is an arbitrary integer denoting the individual defect modes. For further analysis let us assume that the defect is a nonmagnetic homogeneous layer with thickness d_D and refractive index n_D. The THz radiation impinges on the structure under the angle θ_0; we denote by θ_D the angle between the z-axis and the wave vector in the defect layer. Under these assumptions the condition (24) can be transformed into a more specific form:

$$2\tau_{\mathrm{FP}} = 2\pi m - 2\arctan\frac{\tan(\tilde{\rho}_A/2)}{x_D} - 2\arctan\frac{\tan(\rho_B/2)}{x_D} \tag{25}$$

where $\tau_{\mathrm{FP}} = \omega n_D d_D \cos\theta_D / c$ and $x_D = n_D(\cos\theta_D/\cos\theta_0)^k$ ($k = 1$ for the s-polarized beam and $k = -1$ for the p-polarized beam).

Eq. (25) represents the resonance condition in an FP cavity: a constructive FP interference in transmission corresponds to the defect level of the PC. It occurs if the total phase shift for one round trip in the FP cavity equals $2m\pi$. The term $2\tau_{\mathrm{FP}}$ accounts for the phase increase during the propagation through the defect layer while the two last terms

at the right-hand side of Eq. (25) are related to the cumulative phase change due to the reflection on the two Bragg mirrors. A simple term $-(\tilde{\rho}_A + \rho_B)$ at this place would account for the reflectance change observed if both mirrors were placed in the air. The particular form of the last two terms of Eq. (25) then arises from the fact that the resonator is actually formed by the defect material and not by the air layer. These terms thus account for the impedance mismatch between the building blocks and the vacuum. Note that in a standard FP resonator with simple single-layer (e.g. metallic) mirrors these reflectance terms are both equal to π or 0 and do not contribute to the resonance condition.

The tuning of the defect mode position is most easily achieved by changing the parameter τ_{FP}, i.e. the optical thickness of the defect. Let us discuss now the pertinent parameters which define the filtering capabilities and the tunability of the whole PC structure. The desired properties are: a wide forbidden band, a single defect mode inside the forbidden band, high tunability of this mode, high transmission at the defect mode frequency, high quality factor of the filter and compactness and stability of the device.

We restrict our analysis to the case when the Bragg mirrors are formed by alternating layers of two dielectric materials (with refractive indices $n_H > n_L$ and thicknesses d_H and d_L). The highest possible ratio of the forbidden band width to the central angular frequency ω_0 of the bandgap is achieved when the two alternating layers of the Braggs have equal optical thicknesses. This is known in optics as a quarter-wave stack: $\omega_0 = \pi c/d_{tot}$, where d_{tot} is the optical thickness of the unit cell ($d_{tot} = n_H d_H + n_L d_L$). To avoid a large number of modes in the forbidden band it is necessary to keep the optical thickness of the defect layer rather small, i.e., to work with low-order defect modes ($m \lesssim 2$, $\tau_{FP} \lesssim 2\pi$). At the same time a maximum tunability (over the entire forbidden band) can be achieved if the induced change of the defect optical thickness is comparable to the central wavelength $2\pi c/\omega_0$ of the forbidden band (i.e. $\Delta\tau_{FP}$ should not be much smaller than π).

The ordering of the layers constitutes also a very important issue. In our structures we deal with a very low-impedance defect layer (i.e. $n_D \gg n_H, n_L$). A deeper analysis [20] shows that it is then convenient to design the PCs such that the low-index layers of the Braggs are adjacent to the defect (higher impedance mismatch between the defect and the mirrors). If this last condition is fulfilled, the reflectance terms in Eq. (25) are small and the defect mode frequencies approach those of the standard FP cavity surrounded by metallic mirrors. In this situation the defect mode can be tuned over the entire forbidden band; in addition, if the optical thickness of the defect is small—i.e. $m = 0, 1$ as follows from Eq. (25)—a single defect mode appears in the bandgap of PC over virtually entire tuning range (see Fig. 8(a)). The behavior of the defect modes is more complex when the high-index layers are adjacent to the defect: in this case the reflectance terms of Eq. (25) can bring a significant contribution resulting in a pinning of the defect levels close to the center of the band gap (see Fig. 8(b)). The consequence of this behavior is the presence of a larger number of modes within the bandgap (even for small values of m) and a partial suppression of the tunability [20]. Indeed, in Fig. 8(b) one can observe relatively wide intervals where the tuning capability of some defect levels is significantly reduced.

Note that in the THz and GHz spectral ranges the photonic crystals are very frequently made of high-resistivity silicon or quartz as the high-index material; air gaps between the silicon (or quartz) layers then play the role of the low-index material. Following the above reasons the defect layer should be directly surrounded by air gaps for a better performance of the PC. However, this may cause a technical problem in the cases of small or fragile defect. A better solution may consist in finding a suitable high-index material (i.e. with an index of refraction substantially higher than that of silicon) and prepare a compact and mechanically more stable PC without air gaps.

Real defect materials present losses in the THz range. Increasing the reflectivity of Bragg mirrors by employing a higher number of stacked layers leads to the narrowing of the defect mode, but also to an increase of the effective losses in the defect. A compromise thus should be found to obtain a reasonable transmission at the defect mode frequency and a good quality factor. This is achieved using Bragg mirrors with moderately high reflectivity, which implies a relatively small number of bilayers in each Bragg mirror.

4.2. Application using incipient ferroelectrics as defect materials

We have prepared and tested two structures for thermal tuning based on a defect layer made of an incipient ferroelectric material enclosed in a pair of Bragg mirrors [54,25]. The first one was constructed as follows: each Bragg mirror was fabricated using three 100 μm thick (0001)-oriented wafers of crystalline quartz with a 15 mm diameter. Its refractive index ($\approx$2.1) is constant in the THz range and the losses are negligible. The individual wafers were separated by air layers, which were created by inserting 200 μm thick silicon spacers near the edges of the quartz wafers.

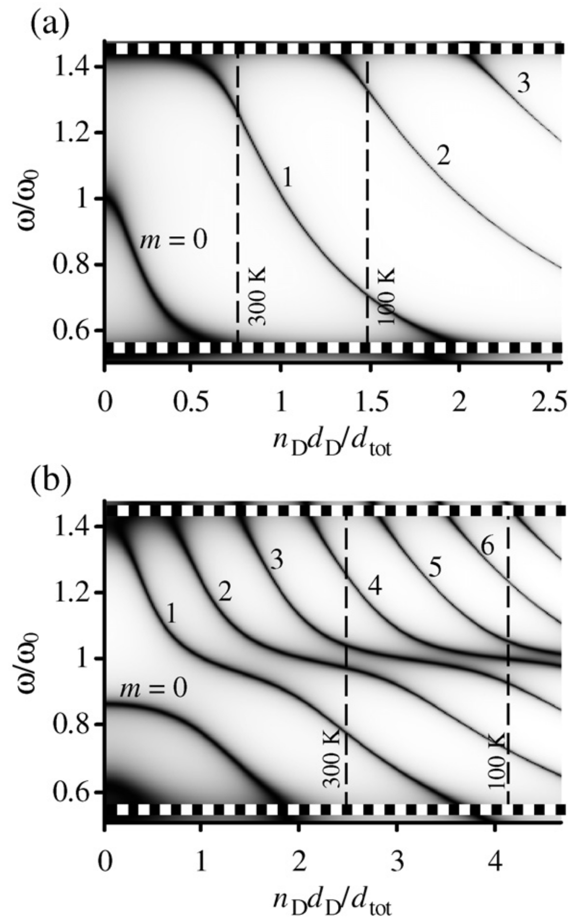

Fig. 8. Frequency of the defect modes versus optical thickness of the defect. The transmittance of the structure is represented by the levels of gray color ($T = 1$ for black color). Thick horizontal dotted bands delimit the bandgap edges and thin vertical dashed lines show the extreme values of the optical thickness of defects for the two photonic crystals studied. We assumed here a tuning of the defect refractive index in the temperature range 100–300 K. (a) Structure according to Fig. 9(a). (b) Three SiO_2 wafers ($d_A = 100$ μm) interleaved with two air layers ($d_B = 210$ μm) form each Bragg mirror; defect layer: KTO ($d_D = 65$ μm). The losses of defect materials are neglected for this model simulation. Note also that $\tau_{FP}(\omega_0) = \pi n_D d_D / d_{tot}$.

These structures were then mechanically stabilized by drops of glue put on their edges. The 65 μm thick KTO defect with a diameter of 7 mm surrounded by a 50 μm thick ring of a Mylar foil was placed between the Bragg mirrors. Finally, the whole structure was fixed by miniature springs. In this setup we expected to minimize the curvature of the PCs caused by the stress produced during the construction or by the springs. The dielectric tunability of KTO at 200 GHz is shown in Fig. 2. The problem with this structure is that thin wafers of KTO are quite fragile and we were not able to prepare a thinner sample; for the same reason (and also due to its lateral size) the KTO defect had to be inserted between two quartz layers and could not be surrounded by air gaps. This leads to several unfavorable conditions which were described in the previous paragraph. The predicted transmission spectra of this structure are shown in Fig. 8(b). In this figure, the range of the relative optical thickness $n_D d_D / d_{tot}$ of the KTO defect, which is available in the 100–300 K temperature range, is delimited by the vertical dashed lines. One observes that four to five modes are present in the bandgap within the temperature range shown. Also the tuning capabilities of modes with $m = 2$, 3 and 4 are inhibited to a large extent (their frequencies are pinned close to ω_0 in a broad range).

In order to improve the performance of the filter we have designed a second structure where several parameters have been improved. As a material very suitable for high-index layers we used undoped high-permittivity CeO_2 ceramics which has a refractive index of 4.8, exhibits very low losses in the THz range and its permittivity shows a negligible temperature dependence [55]. Moreover this material can be quite easily polished to plane parallel plates thinner than

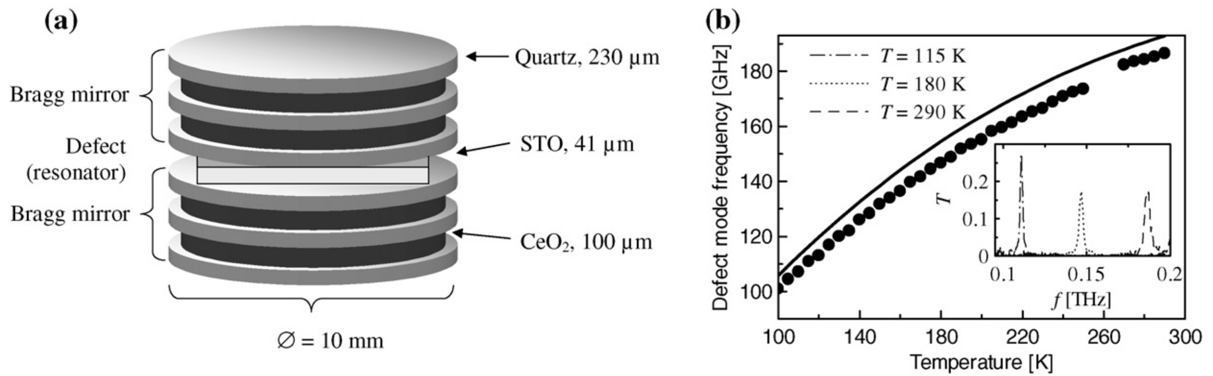

Fig. 9. (a) Scheme of the photonic crystal with STO defect layer used in our studies. (b) Tuning curve of the defect mode of a structure with STO defect layer. Filled circles: measured defect frequency; solid line: results of a numerical simulation. Inset: Typical spectra experimentally obtained in the tuning range.

100 μm. Another improvement consists in the choice of STO as the defect material: in fact, the tunability of STO is somewhat higher than that of KTO while the losses remain comparable at 200 GHz (see Fig. 2); at the same time, STO plates could be polished down to substantially lower thicknesses than KTO ones. As a result we obtained a structure where a single mode (with $m = 1$) was observed in the bandgap exhibiting a tunability over nearly the entire forbidden band (see Fig. 8(a)). This structure (see Fig. 9(a)) was constructed as follows: each Bragg mirror was fabricated of three crystalline quartz wafers (thickness 230 μm, diameter 10 mm) interleaved with two layers of CeO_2 ceramic (thickness 100 μm, diameter 9 mm). The Bragg mirrors were put together by drops of glue at the edges. The defect consisted of a 41 μm thick rectangular (7 × 7 mm) STO single crystal plate. The surfaces of all constituting layers were polished to an optical quality. The entire structure was enclosed between two metallic apertures and tightened with small screws.

The predicted transmission spectra of this structure are shown in Fig. 8(a). The experiments were performed using a backward-wave oscillator spectrometer [56] in the frequency range 67–260 GHz and for temperatures between 75–295 K. In Fig. 9(b), the defect mode frequency is plotted versus temperature. The inset of this figure illustrates the shift of the defect mode frequency for three different temperatures. The defect mode can be tuned from 185 GHz at room temperature down to 100 GHz at 100 K. The relative tunability calculated as the tuning range over the central frequency ω_0 thus reaches an outstanding value of 60%. At the same time, the peak transmission always exceeds −9 dB and the quality factor, defined as the ratio of the defect mode frequency and its full-width-at-half-maximum, exceeds 45 in the whole tuning range. The small systematic discrepancy between the measured and numerically calculated frequencies of the defect mode (Fig. 9(b)) is related to the errors in the determination of structural parameters of the PC.

4.3. Design of a PC with GaAs defect

The main drawback of the modulator described in Section 3 based on photoexcitation of a surface layer in GaAs is that a very high concentration of free electrons is necessary to achieve a full modulation of the THz beam. Consequently, a high-power laser is required. It is possible to introduce a thin GaAs wafer into a 1D PC similar to those discussed in Section 4.1 in order to achieve the THz light modulation at substantially lower free carrier densities.

Let us consider a 1D PC consisting again of two Bragg mirrors and a thin GaAs wafer enclosed between them. Suitably designed structure will show a defect mode close to the center of the forbidden band. In the ground state high-resistivity GaAs is very well transparent for the THz radiation. Consequently the transmittance of the structure at the defect mode frequency will be close to unity. The defect mode of this structure is characterized by a strong enhancement of the electric field inside the defect [20,57]. It means that the interaction of the THz radiation with the defect material is strengthened. A relatively weak photoexcitation of the GaAs wafer will then lead to a substantial decrease of the transmittance at the defect level frequency. As the investigated structure has a resonant character, it allows for a narrow band operation (limited by the spectral width of the defect line) and, consequently, it can be suitable for applications with quasi-monochromatic THz radiation.

We prepared structures which are composed of alternating thin layers of crystalline SiO_2 and MgO with a thin semi-insulating GaAs wafer defect [58,57]. Both SiO_2 and MgO are transparent for the optical frequencies enabling the photoexcitation of the surface of semiconductor. Also the optical refractive indices of these two compounds do not differ much so that the weak delayed optical pulses coming from multiple reflections on SiO_2/MgO interfaces do not significantly contribute to the photoexcitation and can be neglected. The structures were designed for the frequency of 600 GHz which corresponds to the position of the defect mode in the first forbidden band. The FWHM of the defect mode varied between 5 and 16 GHz in the studied structures. The free electron lifetime in our GaAs sample is about 170 ps [57]; this sets the maximum switching rate of the devices to about 5 GHz. Following our estimations and experiments a concentration of free carriers of the order of 10^{15}–10^{16} cm^{-3} in a 1 μm-thick photoexcited layer induces a 50% modulation of the THz transmission of these structures.

5. Conclusion

We have reviewed some of the concepts of devices capable of operation as modulators in the THz frequency range. While the presented structures are, as a rule, easy to fabricate, their operation modes may not yet be optimized for practical use. This is especially true for the temperature tuning which requires the whole photonic crystal to be cooled down. Although such an approach is less convenient for most applications, it appeared in turn useful for validating the idea of exploiting a photonic crystal with a defect where the dielectric properties are controlled by an external parameter; the advantage consists in the fact that in the experiments, the temperature can be easily stabilized with a high precision. Consequently, the temperature controlled devices may still be employed in laboratory conditions. The other control parameters discussed in our review, i.e. light illumination and electric field, improve the tuning possibilities by enabling a potentially very fast control of the THz wave propagation, which might have an impact on the future applications in the THz communications. In this context, the tuning by an external electric bias is of particular interest as a cost-effective solution. In summary, we believe that the effort of developing novel tunable devices tunable in the THz range has the potential to bring solutions meeting the needs of emerging markets using the THz technology.

Acknowledgements

We are thankful to N. Klein, L. Duvillaret and H. Němec for their very important contribution to the work presented in this paper and also to J. Petzelt for very helpful discussions. The support by Ministry of Education of the Czech Republic (project LC512) and by the Grant Agency of the Academy of Sciences of the Czech Republic (project KJB100100512) is also acknowledged.

References

[1] M.C. Nuss, J. Orenstein, Terahertz time-domain spectroscopy, in: Millimeter and Submillimeter Wave Spectroscopy of Solids, Springer-Verlag, Berlin/Heidelberg, 1998, pp. 7–50 (Chapter 2).
[2] D. Mittleman, Sensing with Terahertz Radiation, Springer-Verlag, Berlin, 2003.
[3] B. Ferguson, X.-C. Zhang, Nature Mater. 1 (2002) 26.
[4] M.E. Lines, A.M. Glass, Principles and Applications of Ferroelectrics and Related Materials, Oxford University Press, 1977.
[5] A.K. Tagantsev, V.O. Sherman, K.F. Astafiev, J. Venkatesh, N. Setter, J. Electroceram. 11 (2003) 5.
[6] J.H. Haeni, P. Irvin, W. Chang, R. Uecker, P. Reiche, Y.L. Li, S. Choudhury, W. Tian, M.E. Hawley, B. Craigo, A.K. Tagantsev, X.Q. Pan, S.K. Streiffer, L.Q. Chen, S.W. Kirchoefer, J. Levy, D.G. Schlom, Nature 430 (2004) 758.
[7] K.C. Lim, J.D. Margerum, A.M. Lackner, Appl. Phys. Lett. 62 (1993) 1065.
[8] C.-Y. Chen, T.-R. Tsai, C.-L. Pan, R.-P. Pan, Appl. Phys. Lett. 83 (2003) 4497.
[9] C.-Y. Chen, C.-F. Hsieh, Y.-F. Lin, R.-P. Pan, C.-L. Pan, Opt. Express 12 (2004) 2630.
[10] C.-Y. Chen, C.-L. Pan, C.-F. Hsieh, Y.-F. Lin, R.-P. Pan, Appl. Phys. Lett. 88 (2006) 101107.
[11] C.-F. Hsieh, R.-P. Pan, T.-T. Tang, H.-L. Chen, C.-L. Pan, Opt. Lett. 31 (2006) 1112.
[12] A. Chelnokov, S. Rowson, J.-M. Lourtioz, L. Duvillaret, J.-L. Coutaz, Electron. Lett. 34 (1998) 1965.
[13] I.H. Libon, S. Baumgärtner, M. Hempel, N.E. Hecker, J. Feldmann, M. Koch, P. Dawson, Appl. Phys. Lett. 76 (2000) 2821.
[14] L. Fekete, J.Y. Hlinka, F. Kadlec, P. Kužel, P. Mounaix, Opt. Lett. 30 (2005) 1992.
[15] T. Kleine-Ostmann, P. Dawson, K. Pierz, G. Hein, M. Koch, Appl. Phys. Lett. 84 (2004) 3555.
[16] H.-T. Chen, W.J. Padilla, J.M.O. Zide, A.C. Gossard, A.J. Taylor, R.D. Averitt, Nature 444 (2006) 597.
[17] H.-T. Chen, W.J. Padilla, J.M.O. Zide, S.R. Bank, A.C. Gossard, A.J. Taylor, R.D. Averitt, Opt. Lett. 32 (2007) 1620.

[18] K. Sakoda, Optical Properties of Photonic Crystals, Springer, Berlin, 2001.
[19] E. Özbay, B. Temelkuran, Appl. Phys. Lett. 69 (1996) 743.
[20] H. Němec, L. Duvillaret, F. Quemeneur, P. Kužel, J. Opt. Soc. Am. B 21 (2004) 548.
[21] M. Inoue, K. Arai, T. Fujii, M. Abe, J. Appl. Phys. 85 (1999) 5768.
[22] Y. Lai, W. Zhang, L. Zhang, J.A.R. Williams, I. Bennion, Opt. Lett. 28 (2003) 2446.
[23] B. Wild, R. Ferrini, R. Houdré, M. Mulot, S. Anand, C.J.M. Smith, Appl. Phys. Lett. 84 (2004) 846.
[24] R. Ozaki, Y. Matsuhisa, M. Ozaki, K. Yoshino, Appl. Phys. Lett. 84 (2004) 1844.
[25] H. Němec, P. Kužel, L. Duvillaret, A. Pashkin, M. Dressel, M. Sebastian, Opt. Lett. 30 (2005) 549.
[26] N. Krumbholz, K. Gerlach, F. Rutz, M. Koch, R. Piesiewicz, T. Kürner, D. Mittleman, Appl. Phys. Lett. 88 (2006) 202905.
[27] P. Kužel, J. Petzelt, Ferroelectrics 239 (2000) 949.
[28] M. Kempa, P. Kužel, S. Kamba, P. Samoukhina, J. Petzelt, A. Garg, Z. Barber, J. Phys.: Condens. Matter 15 (2003) 8095.
[29] H. Němec, P. Kužel, F. Garet, L. Duvillaret, Appl. Opt. 43 (2004) 1965.
[30] F. Kadlec, H. Němec, P. Kužel, Phys. Rev. B 70 (2004) 125205 1.
[31] P.A. Fleury, J.M. Worlock, Phys. Rev. 174 (1968) 613.
[32] Y. Yamada, G. Shirane, J. Phys. Soc. Jpn. 26 (1969) 396.
[33] A. Yamanaka, M. Kataoka, Y. Inaba, K. Inoue, B. Hehlen, E. Courtens, Europhys. Lett. 50 (2000) 688.
[34] I. Fedorov, V. Železný, J. Petzelt, V. Trepakov, M. Jelínek, V. Trtík, M. Čerňanský, V. Studnička, Ferroelectrics 208–209 (1998) 413.
[35] A.A. Sirenko, C. Bernhard, A. Golnik, A.M. Clark, J. Hao, W. Si, X.X. Xi, Nature (London) 404 (2000) 373.
[36] Y.I. Yuzyuk, V.A. Alyoshin, I.N. Zakharchenko, E.V. Sviridov, A. Almeida, M.R. Chaves, Phys. Rev. B 65 (2002) 134107.
[37] T. Ostapchuk, J. Petzelt, V. Železný, A. Pashkin, J. Pokorný, I. Drbohlav, R. Kužel, D. Rafaja, B.P. Gorshunov, M. Dressel, C. Ohly, S. Hoffmann-Eifert, R. Waser, Phys. Rev. B 66 (2002) 235406.
[38] J. Petzelt, P. Kužel, I. Rychetský, A. Pashkin, T. Ostapchuk, Ferroelectrics 288 (2003) 169.
[39] J. Petzelt, T. Ostapchuk, I. Gregora, I. Rychetský, S. Hoffmann-Eifert, A.V. Pronin, Y. Yuzyuk, B.P. Gorshunov, S. Kamba, V. Bovtun, J. Pokorný, M. Savinov, V. Porokhonskyy, D. Rafaja, P. Vanek, A. Almeida, M.R. Chaves, Phys. Rev. B 64 (2001) 184111.
[40] M. Misra, K. Kotani, I. Kawayama, H. Murakami, M. Tonouchi, Appl. Phys. Lett. 87 (2005) 182909.
[41] J.L. Servoin, Y. Luspin, F. Gervais, Phys. Rev. B 22 (1980) 5501.
[42] H. Vogt, G. Rossbroich, Phys. Rev. B 24 (1981) 3086.
[43] J. Petzelt, T. Ostapchuk, I. Gregora, S. Hoffmann, J. Lindner, D. Rafaja, S. Kamba, J. Pokorný, V. Bovtun, V. Porokhonsky, M. Savinov, P. Vanek, I. Rychetský, V. Perina, R. Waser, Integr. Ferroelectrics 32 (2001) 11.
[44] J. Petzelt, T. Ostapchuk, S. Kamba, I. Rychetský, M. Savinov, A. Volkov, B. Gorshunov, A. Pronin, S. Hoffmann, R. Waser, J. Lindner, Ferroelectrics 239 (2000) 117.
[45] J. Li, Opt. Commun. 269 (2007) 98.
[46] O.G. Vendik, S.P. Zubko, J. Appl. Phys. 88 (2000) 5343.
[47] M. Born, E. Wolf, Principles of Optics, seventh ed., University Press, Cambridge, 2003.
[48] P. Kužel, F. Kadlec, H. Němec, R. Ott, E. Hollmann, N. Klein, Appl. Phys. Lett. 88 (2006) 102901.
[49] T. Nozokido, H. Minamide, K. Mizuno, Electron. Comm. Jpn. II 80 (1997) 1.
[50] C. Karaalioglu, I.-C.A. Chen, M. Brucherseifer, A. Meshal, R. Martini, Proc. SPIE 5790 (2005) 263.
[51] S. Biber, D. Schneiderbanger, L.-P. Schmidt, Frequenz 59 (2005) 141.
[52] N.W. Ashcroft, N.D. Mermin, Solid State Physics, Holt, Rinehart and Winston, New York, 1976.
[53] R. Jacobsson, Light reflection from films of continuously varying refractive index, in: Progress in Optics, vol. V, North-Holland, Amsterdam, 1965 (Chapter 5).
[54] H. Němec, L. Duvillaret, F. Garet, P. Kužel, P. Xavier, J. Richard, D. Rauly, J. Appl. Phys. 96 (2004) 4072.
[55] N.L. Santha, M.T. Sebastian, P. Mohanan, N.M. Alford, K. Sarma, R.C. Pullar, S. Kamba, A. Pashkin, P. Samukhina, J. Petzelt, J. Am. Ceram. Soc. 87 (2004) 1233.
[56] G. Grüner (Ed.), Millimeter and Submillimeter Wave Spectroscopy of Solids, Springer-Verlag, Berlin/Heidelberg, 1998.
[57] L. Fekete, F. Kadlec, H. Němec, P. Kužel, Opt. Express 15 (2007) 8898.
[58] L. Fekete, F. Kadlec, P. Kužel, H. Němec, Opt. Lett. 32 (2007) 680.